JGR Atmospheres

Correspondence to:
T. J. Anurose
anurostj@gmail.com

Understanding the Moisture Variance in Precipitating Shallow Cumulus Convection

T. J. Anurose[1] , **Ivan Bašták Ďurán[1]** , **Juerg Schmidli[1]** , and **Axel Seifert[2]**

[1]Institute for Atmospheric and Environmental Sciences, Goethe-University, Frankfurt am Main, Germany, [2]Deutscher Wetterdienst, Offenbach, Germany

Abstract The impact of precipitation in shallow cumulus convection on the moisture variance and third-order moments of moisture is investigated with the help of large-eddy simulations. Three idealized simulations based on the Rain in Cumulus over the Ocean field experiment are analyzed: one nonprecipitating, on a smaller domain, and two precipitating cases, on a larger domain with different initial profiles of moisture. Results show that precipitation and the associated cloud organization lead to increased generation of higher-order moments (HOM) of moisture compared to the nonprecipitating case. To understand the physical mechanism and the role of individual processes in this increase, budgets of HOM of moisture are studied. Microphysics directly decreases the generation of HOM of moisture, but this effect is not dominant. The gradient production term is identified as the main source term in the HOM budgets. The influence of the gradient production term on moisture variance is further examined separately in cloud active and nonactive regions. The main contribution to the gradient production term comes from the smaller cloud active region because of the stronger moisture flux. Further analyses of the horizontal and vertical cross sections of moisture fluctuations show that the precipitation-induced downdrafts and updrafts are the main mechanism for the generation of moisture variance. The variance increase is linked to shallow dry downdraft regions with horizontal divergence in the subcloud layer, moist updrafts with horizontal convergence in the bulk cloud layer, and finally wider areas of horizontal divergence in the cloud inversion layer.

1. Introduction

Shallow cumulus clouds are frequently observed over the world oceans, especially over large parts of the trade wind regions. They strongly influence mixing processes in the lower atmosphere, and they modulate the radiative energy budget at the Earth's surface. In numerical weather prediction models, it is often (with few exceptions) assumed that they are nonprecipitating. However, observational studies show that trade wind cumuli precipitate frequently, which has drawn much attention in recent years (Matheou et al., 2011; Nuijens et al., 2003; Rauber et al., 2007; Short & Nakamura, 2000; Siebesma et al., 2003; van Zanten et al., 2011).

Precipitation from shallow cumulus clouds is important, because it may lead to cloud organization on larger scales, for example, the formation of cloud clusters or mesoscale arcs (Bretherton & Blossey, 2017; Seifert & Heus, 2013; Snodgrass et al., 2009). The resulting cloud organization in turn changes the environmental properties and modifies the complex interactions among different physical processes within the cloud-topped boundary layer. The bulk cloud properties and the cloud organization are interlinked. For example, cloud formation leads to vertical transport of moist air and creates localized moisture perturbations; if the upward transported moisture falls out as precipitation, it can induce the formation of cold pools and create further moisture anomalies with specific patterns. These anomalies can initiate further convective activity and so result in the organization of clouds.

For modeling, it is necessary to understand and describe the above complex feedback mechanisms, but it might prove difficult to do it on the level of the individual processes. Instead, it may be more convenient to find a relationship between cloud organization and the properties of clouds, intensity of convection, and occurrence of precipitation. Numerous studies have shown that presence of cloud organization is connected to higher-order moments (HOMs) of the turbulent quantities (e.g., moisture, temperature, and velocity) and that these variables can provide useful insight about the characteristics of convective and cloud-topped

boundary layers (Bodine et al., 2010; Couvreux et al., 2005; Couvreux et al., 2007; Mahrt, 1991; Mellado et al., 2017; Neggers et al., 2007; Weckwerth, 2000). Concerning the relationship between organization and the scalar HOMs (moisture and temperature), one can argue that the scalar HOMs are not always directly linked to organization and can exist independently of the systematic organization of convection. For example, the scalar HOM can peak at the level of maximum gradient near the inversion region (Deardorff, 1974; Neggers et al., 2007). However, it is evident that the presence of cloud organization often increases the magnitudes of HOMs (Roode et al., 2004; Schemann & Seifert, 2017; Seifert & Heus, 2013). The importance of the scalar HOMs for the dynamics of the flow is obvious from the Reynolds-averaged basic equations (Stull, 1988); hence, they play a vital role in boundary layer parametrization. They are either implicitly present in the parameterization or they are explicitly represented and treated as prognostic quantities (Bogenschutz & Krueger, 2013; Cheng & Xu, 2015; Golaz et al., 2001; Lappen & Randall, 2001; Larson & Golaz, 2005; Mellor & Yamada, 1974; Mellor & Yamada, 1982; Moeng & Wyngaard, 1989). Thus, there is a possibility (in particular in the latter case) to introduce the effect of cloud organization into current parametrization schemes via the HOMs of moisture. This requires a proper understanding of the feedback mechanisms between the HOMs of moisture, precipitation, and cloud organization for precipitating shallow convection.

Observational and numerical studies during the last couple of decades have provided considerable insight into the second- and third-order moments (TOMs) of moisture related to both free and cloud-topped boundary layers (Cuijpers et al., 1996; Moeng & Wyngaard, 1989; Wulfmeyer, 1999). For a convective boundary layer (CBL), Couvreux et al. (2007) underlines the link between convective activity and moisture by a comprehensive analysis of the moisture variance, the TOMs, and skewness budgets. Neggers et al. (2007) explains the complex vertical structure of moisture variance and its relationship with the transition zone under different shallow cumulus cases. For stratocumulus convection, Zhou et al. (2017) show that microphysics amplifies subcloud moisture variances and changes the dynamics in the subcloud layer (SCL), while it does not affect the mesoscale organization of the cloud layer.

These studies are for nonprecipitating cases. For precipitating shallow cumulus convection, it has been demonstrated that an increase of moisture variance occurs as a result of precipitation and cloud clustering (Bretherton & Blossey, 2017; Griffin & Larson, 2016; Schemann & Seifert, 2017; Seifert & Heus, 2013). But there remain many open questions regarding the source mechanism of moisture variance and the associated variance-precipitation feedback. Also, the correlation of moisture skewness with cloud organization has not yet been thoroughly examined. In this regard, the main goal of the present paper is to perform a detailed analysis of the moisture variance in a precipitating cloud-topped boundary layer and thereby investigate the complex interplay between precipitation, cloud organization, and moisture variance. The study complements previous work by Schemann and Seifert (2017), where the moisture variance budget is analyzed with an emphasis on the cloud microphysics and its parameterization. Here the main focus is on the generation of moisture variance, the physical mechanisms driving it, and how it is influenced by the vertical structure of the boundary layer. The relative role of precipitation-induced updrafts and downdrafts versus the direct effects of cloud microphysics (e.g., evaporation) will be examined in detail. Additionally, the connection between cloud organization and the TOM of moisture will be investigated.

Our study requires quality data with high resolution, which can be provided by the means of large-eddy simulation (LES). Hence, a precipitating shallow cumulus case is run with high resolution (25 m) for a large domain (50 km). The temporal evolution and the budgets of the HOMs of moisture will be investigated. Then, with the aim to understand the underlying dynamics, the conditional behavior and spatial distribution of the source and sink terms in the budgets will be examined.

The remainder of the paper is organized as follows. Section 2 outlines the LES model and the simulation setup together with the methodology used for the data analysis. The results and their interpretations are presented in section 3. Section 4 concludes with a summary and discussion of the main findings.

2. Model and Methodology

2.1. Experimental Setup

The numerical model used in the study is the LES model MicroHH (van Heerwaarden et al., 2017a). MicroHH is a three-dimensional computational fluid dynamics code developed for direct numerical simulation and LES of turbulent flows in the atmosphere. The dynamics of MicroHH uses a fully conservative second-order finite difference scheme in space and a third-order Runge-Kutta scheme in time. The model

Table 1
Details of LES Experiments

Name	Domain size (km)	Number of grid points in x, y, and z direction	Simulation time (hr)	Initial conditions
STD	$50 \times 50 \times 6$	$2,000 \times 2,000 \times 240$	60	GCSS
MST	$50 \times 50 \times 6$	$2,000 \times 2,000 \times 240$	60	GCSS + 2 g kg^{-1} in the cloud layer and above
CTRL	$8 \times 8 \times 6$	$320 \times 320 \times 240$	60	GCSS

Note. Vertical and horizontal grid spacing for all experiments is 25 m.

solves the filtered Navier-Stokes equations with the anelastic approximation applied on a staggered grid. The lower boundary condition is based on Monin-Obukhov similarity theory. The subfilter-scale fluxes are derived by a Smagorinsky-Lilly scheme (Lilly, 1968). In the present study, MicroHH is used in LES configuration with moist physics (see below). The lateral boundary conditions are periodic.

Three idealized simulations are analyzed in this paper (see Table 1). The experimental setup is based on the Rain in Cumulus over the Ocean (RICO) field experiment as used in the GEWEX Cloud System Study RICO model intercomparison study (Rauber et al., 2007; van Zanten et al., 2011). The experiment, defined as the standard case (referenced as STD in the figures), uses the GEWEX Cloud System Study configuration, while the second experiment, termed as the moist case (referenced as MST in the figures), is initialized with an increased moisture content in the cloud layer and above of about $\sim$2 g kg^{-1}. The main idea behind the moist case simulation is to support a faster formation of precipitation (Seifert & Heus, 2013). The configuration of the standard and moist cases is similar to the setup described in Seifert and Heus (2013). Both of these experiments cover a domain size of $50 \times 50 \times 6$ km with an isotropic grid spacing of 25 m. The control simulation, referenced as CTRL in the figures, is a nonprecipitating reference simulation. The setup for the control case is identical to the setup of the standard case, except for a smaller domain size of $8 \times 8 \times 6$ km. The relatively small domain for the control case is chosen in order to inhibit the organization of clouds into mesoscale structures and thereby prevent the formation of rain. In previous studies, the inhibition of cloud organization was achieved by modifying the cloud droplet number density (Schemann & Seifert, 2017; Seifert et al., 2015; Seifert & Heus, 2013). The simulations are run for 60 hr in all three cases with an adaptive time step of the order of 1 s. Large-scale forcings for temperature, moisture, and radiation as well as large-scale subsidence are prescribed. The surface fluxes are calculated using bulk aerodynamic equations. Cloud microphysical processes are calculated based on the two-moment warm rain scheme of Seifert and Beheng (2001). The cloud droplet concentration is set to 70 cm^{-3} (within clouds).

2.2. Data Analysis

The aim of the paper is to analyze the processes associated with the generation of moisture variance and skewness in precipitating shallow convection. The previous studies focused on the analysis of the whole atmospheric boundary layer (ABL). In order to better understand the vertical distribution of the processes, we distinguish between three sublayers of the ABL: the SCL, the bulk cloud layer (BCL), and the cloud inversion layer (CIL). These layers are defined using the cloud liquid water, q_l, profile (see Figure 3). The SCL is the layer from the surface up to the cloud base, defined as the altitude where q_l becomes greater than 10^{-3} mg/kg. The BCL is the region that extends from the cloud base to the altitude where q_l reaches its maximum. The CIL extends from the q_l peak to the altitude where q_l becomes zero ($\sim$4 km).

Conditional spatial averaging is performed in order to understand the significance of the convective regions in the generation of moisture variance. The conditional averages are defined as cloud active (CA) and non-active (NA) (Bastak Duran et al., 2018). The CA region is defined by averaging all grid points that have at least one active vertical level in the column, which is a level that has nonzero liquid cloud water, is positively buoyant, and has a positive vertical velocity (updraft). Then the NA region refers to the grid points which are not CA. The mean profiles used in the study are calculated based on a 5-hr temporal average, 30–35 hr. This time period is chosen because both the standard and moist simulations have reached a quasi-equilibrium steady state, while the control simulation remains nonprecipitating. The snapshots presented in the paper are for $t = 35$ hr.

2.3. Budget Equations

To understand the source, sink, and transport processes of moisture variance, we analyze the moisture variance budget. The budget equations are derived using the Reynolds-averaging rules in conjunction with incompressibility and horizontal homogeneity assumptions (Stull, 1988). The budget equation for the variance of moisture $(\overline{q_t'^2})$ homogeneous ABL is given by (Stull, 1988)

$$\frac{\partial \overline{q_t'^2}}{\partial t} = \underbrace{-2\overline{q_t'w'}\frac{\partial \overline{q_t}}{\partial z}}_{\text{I}} - \underbrace{\frac{\partial \overline{w'q_t'^2}}{\partial z}}_{\text{II}} + \underbrace{2\overline{q_t'Q_{q_t}}}_{\text{III}} - \underbrace{2\epsilon_{qt}^x}_{\text{IV}}. \tag{1}$$

Term I represent the gradient production of moisture variance, and Term II represent the turbulent transport of moisture variance. Term III is the microphysics term. The microphysical tendency of q_t, Q_{q_t}, consists of three components corresponding to the microphysical processes of accretion, autoconversion, and evaporation (see further details in Schemann and Seifert (2017). Term IV is the dissipation rate. The Smagorinsky-Lilly SGS model is used for the computation of the dissipation term in MicroHH-LES, which yields the following expression:

$$\epsilon_{qt}^x = \overline{K_h \left[\left(\frac{\partial q_t'}{\partial x}\right)^2 + \left(\frac{\partial q_t'}{\partial y}\right)^2 + \left(\frac{\partial q_t'}{\partial z}\right)^2 \right]}, \tag{2}$$

where K_h is the eddy diffusivity for moisture and heat. It is obtained from $K_h = K_m/Pr$, where K_m is the eddy diffusivity for momentum and Pr is the turbulent Prandtl number (set to $\frac{1}{3}$ in MicroHH).

In addition, a conditional budget analysis for specific spatial regions (CA and NA) is carried out. This requires adding the horizontal advection and turbulent transport terms to the budget equation (1), resulting in

$$\frac{\partial \overline{q_t'^2}}{\partial t} = \underbrace{-2\overline{q_t'w'}\frac{\partial \overline{q_t}}{\partial z}}_{\text{I}} - \underbrace{\frac{\partial \overline{w'q_t'^2}}{\partial z}}_{\text{II}} + \underbrace{2\overline{q_t'Q_{q_t}}}_{\text{III}} - \underbrace{2\epsilon_{qt}^x}_{\text{IV}} - \underbrace{\overline{u}\frac{\partial \overline{q_t'^2}}{\partial x} - \overline{v}\frac{\partial \overline{q_t'^2}}{\partial y}}_{\text{V}} - \underbrace{\frac{\partial \overline{u'q_t'^2}}{\partial x} - \frac{\partial \overline{v'q_t'^2}}{\partial y}}_{\text{VI}}. \tag{3}$$

Here the overbar corresponds to an average in time (as before) and over a certain spatial region (CA or NA). Terms V and VI represent the horizontal advection and turbulent transport components, respectively. The remaining horizontal components are assumed to be small and are not included in the present analysis.

The organization of clouds can be linked to the TOM of q_t', which compared to $\overline{q_t'^2}$ has additional information about the skewness of the total water distribution. Therefore, we will also analyze $\overline{q_t'^3}$ and its budget. The budget equation for the TOM of moisture $(\overline{q_t'^3})$ is

$$\frac{\partial \overline{q_t'^3}}{\partial t} = \underbrace{-3\overline{q_t'^2w'}\frac{\partial \overline{q_t}}{\partial z}}_{\text{I}} - \underbrace{\frac{\partial \overline{w'q_t'^3}}{\partial z}}_{\text{II}} + \underbrace{3\overline{q_t'^2Q_{q_t}}}_{\text{III}} - \underbrace{6\epsilon_{qt}^y}_{\text{IV}} + \underbrace{3\overline{q_t'^2}\frac{\partial \overline{w'q_t'}}{\partial z}}_{\text{V}}. \tag{4}$$

Term I represent the gradient production of $\overline{q_t'^3}$, and Term II represent the turbulent transport of $\overline{q_t'^3}$. Term III is the microphysics term, and Term V is the flux divergence term. Term IV is the dissipation rate and is calculated by the following expression:

$$\epsilon_{qt}^y = \overline{K_h \left[q_t' \left(\frac{\partial q_t'}{\partial x}\right)^2 + q_t' \left(\frac{\partial q_t'}{\partial y}\right)^2 + q_t' \left(\frac{\partial q_t'}{\partial z}\right)^2 \right]}. \tag{5}$$

Approximations to the ensemble-mean budgets can be derived from the LES by averaging the data horizontally and then averaging the resulting profiles over several hundred time steps (a minimum of 5-10 large-eddy time scales Heinze et al., 2015). Thus, the budget terms are calculated by horizontally averaging the LES data over the entire domain and then temporally averaging over the 5 hr time period between 30 and 35 hr (sampling time of 1 min). Since the spatial resolution is sufficiently high, subgrid scale contributions to the budget terms are neglected with the exception of dissipation as in Schemann and Seifert (2017). The residuals are defined as the sum of all terms. It is a measure of the unsteadiness and/or approximation errors to the budget terms.
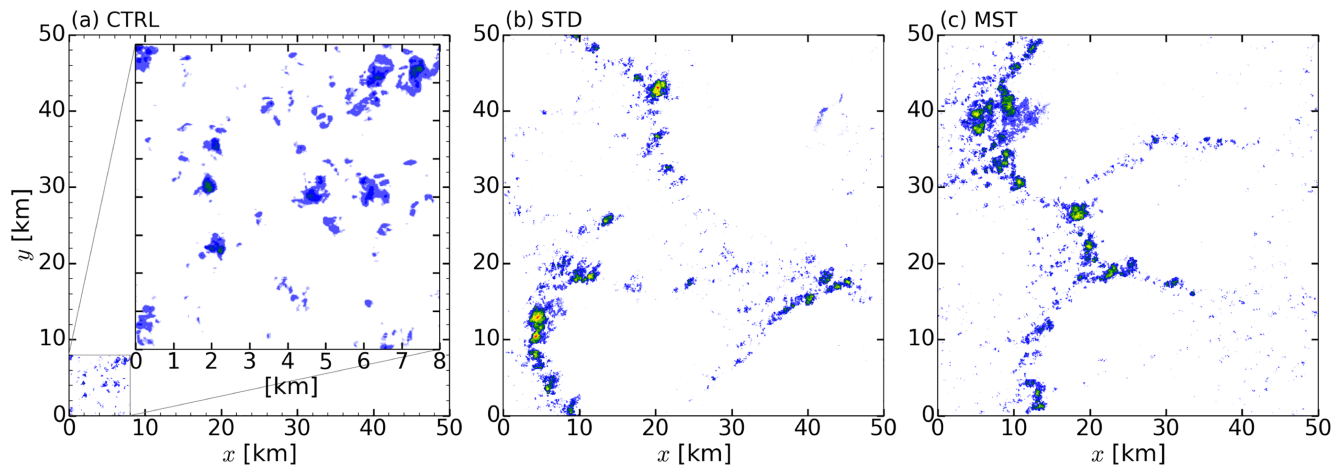
Figure 1. Snap shots of the cloud liquid water path for the three experiments (after 34 hr of simulation): (a) CTRL, (b) STD, and (c) MST. The snapshot is plotted for the 8 × 8 km domain for CTRL and also zoomed out for comparison with the other two large-domain experiments.

3. Results

### 3.1. Cloud Characteristics: Overview of the Simulations

To demonstrate the evolution of simulated cloud fields, we show horizontal snapshots of cloud liquid water path in Figure 1. As expected, the control case displays small random cloud structures without cloud organization, whereas both the standard and the moist precipitating cases exhibit mesoscale arc structures, a typical feature of organized precipitating shallow cumulus clouds (e.g. Seifert & Heus, 2013; Snodgrass et al., 2009). The temporal evolution of different cloud diagnostics (rain water path, liquid water path, and cloud cover) is shown in Figure 2, and the corresponding mean vertical profiles of cloud fraction and cloud liquid water content are depicted in Figure 3. To complete the picture, the profiles of virtual potential temperature are also shown in Figure 3. The cloud diagnostics illustrates the impact of precipitation on the cloud fields and corresponding bulk properties of the ABL. After the onset of precipitation, the cloud cover and the liquid water path decrease significantly (see STD and MST) and remain approximately constant after 30 hr.

The impact of the rain on the vertical structure of the cloud layer is visible mainly in the shape and extent of the CIL. In the nonprecipitating control case, there is only limited transport across the stable layer on top of the boundary layer, which is visible from the vertical profile of virtual potential temperature (θ_v). Hence, the CIL is very shallow, and a sharp peak in cloud liquid water (q_l) and cloud cover (C) separates the BCL from the CIL. With the onset of precipitation (STD and MST), convection is able to locally penetrate the stable layer and transport more air from the BCL to the expanding CIL (Nuijens et al., 2003). In this process, the BCL decreases in depth, and the differences of q_l, C, and θ_v between the BCL and the CIL are reduced. Overall, the general characteristics of the cloud fields from our LES experiments are consistent with previous research and observations (Matheou et al., 2011; Seifert et al., 2015; Seifert & Heus, 2013; van Zanten et al., 2011).

3.2. Analysis of the Moisture Variance and the TOM of Moisture
3.2.1. Quasi-Steady State

Precipitation influences the moisture variance ($\overline{q_t'^2}$) and the TOM of moisture ($\overline{q_t'^3}$). Their profiles in the quasi-steady state (after 30 hr of integration) are depicted in Figure 4. Precipitation leads to a substantial increase of $\overline{q_t'^2}$ throughout the profile for both precipitating cases in comparison with the control case, except for regions of strong moisture gradients in the control case (at the interfaces between the layers). The profiles of $\overline{q_t'^3}$ resemble the structure of the variance profiles, except in the lower part of the SCL. There, the distribution of q_t is negatively skewed. According to Mahrt (1991), the negative values of moisture skewness near the surface is an indicator of entrainment drying of the boundary layer, and the positive values are related to the moistening regime. Past observations and LES experiments for the nonprecipitating boundary layer have shown that negative values of $\overline{q_t'^3}$ are related to tongues of dry air penetrating from the free atmosphere deep into the CBL (Couvreux et al., 2005; Couvreux et al., 2007; Mahrt, 1991; Mellado et al., 2017; Turner et al., 2014). We observe the same behavior for the precipitating and cloudy environment (Figure 4b), where the negative $\overline{q_t'^3}$ values are associated with downdrafts of dry air into the SCL. We further examine
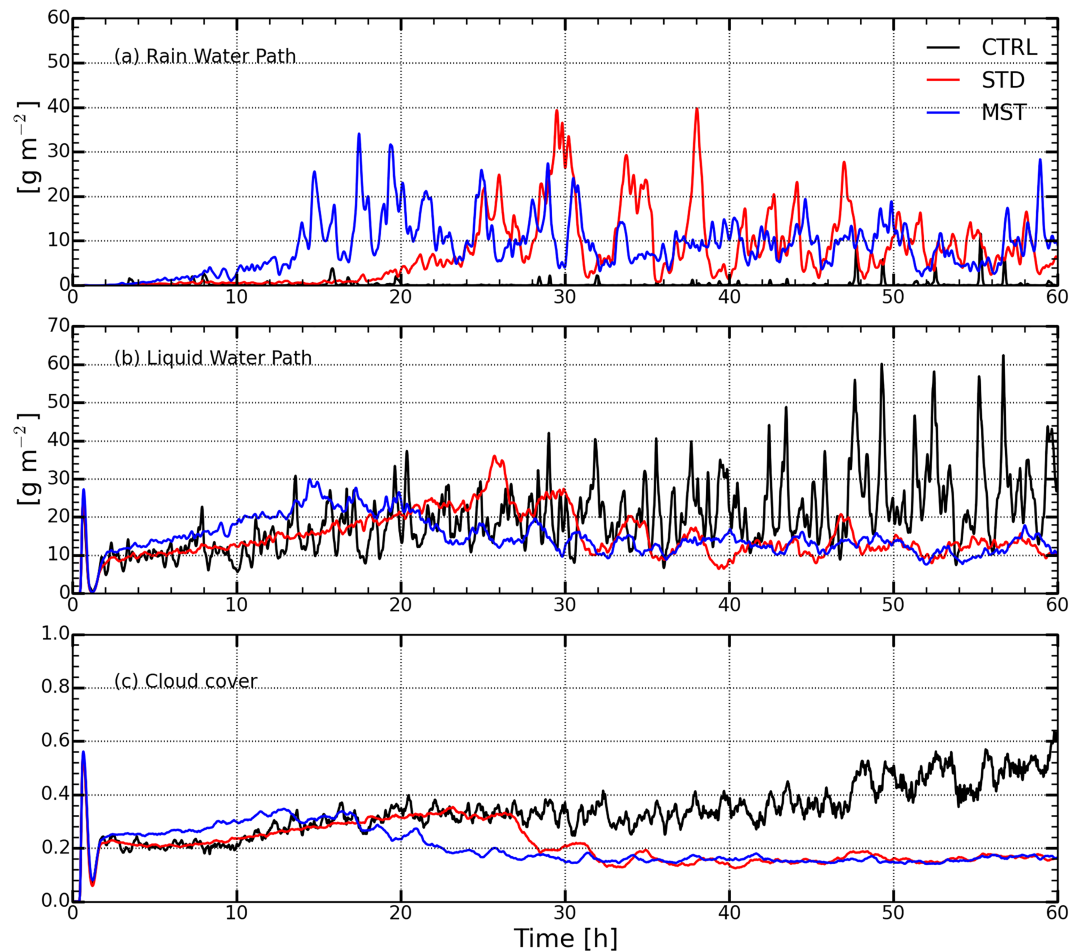
Figure 2. Time series of the domain-averaged (a) rain water path, (b) liquid water path, and (c) cloud cover for the three experiments.

these aspects with the help of horizontal cross sections of the moisture distribution and the wind field in section 3.3. The relatively large positive and negative values of $\overline{q_t'^3}$ for the precipitating cases indicate a more asymmetric distribution of the moisture perturbations.

3.2.2. Temporal Evolution

The CBL undergoes several changes before the simulations attain a quasi-steady state. To study the evolution of the HOMs of moisture during the onset of cloud organization and precipitation, we analyze the time series of the moisture variance and the TOM of moisture averaged over the entire vertical column in Figure 5 (see Total). Since the magnitude of $\overline{q_t'^2}$ varies in the vertical, we also show the time series of the second-order moment and TOM of moisture vertically averaged over the three distinct sublayers: SCL, BCL, and CIL. There are three different regimes in the evolution of the moisture variance (Figure 2): an initial regime, prior to the onset of precipitation; a transition regime, starting with the onset of precipitation; and a quasi-steady regime, where the microphysical processes are balanced with the remaining terms in the $\overline{q_t'^2}$ budget equation. The total moisture variance is similar for all simulations in the initial regime, the variance increases during the transition period (for the precipitating cases) and remains quasi-steady afterward. The transition period starts later for the standard case (~25 hr) than for the moist case (~15 hr), but the standard case attains higher values of the moisture variance in the quasi-steady state. The quasi-steady state oscillations of the moisture variance are also larger for the standard case. The biggest contribution to the moisture variance is located in the CIL. We examine these differences further in section 3.3. Differences between the precipitating cases are also visible in the SCL and BCL but are of smaller magnitude. Compared to the standard precipitating case, the magnitude of the TOM of moisture is very small for the control and the moist case. For the standard case, the major generation of moisture skewness is in the CIL.
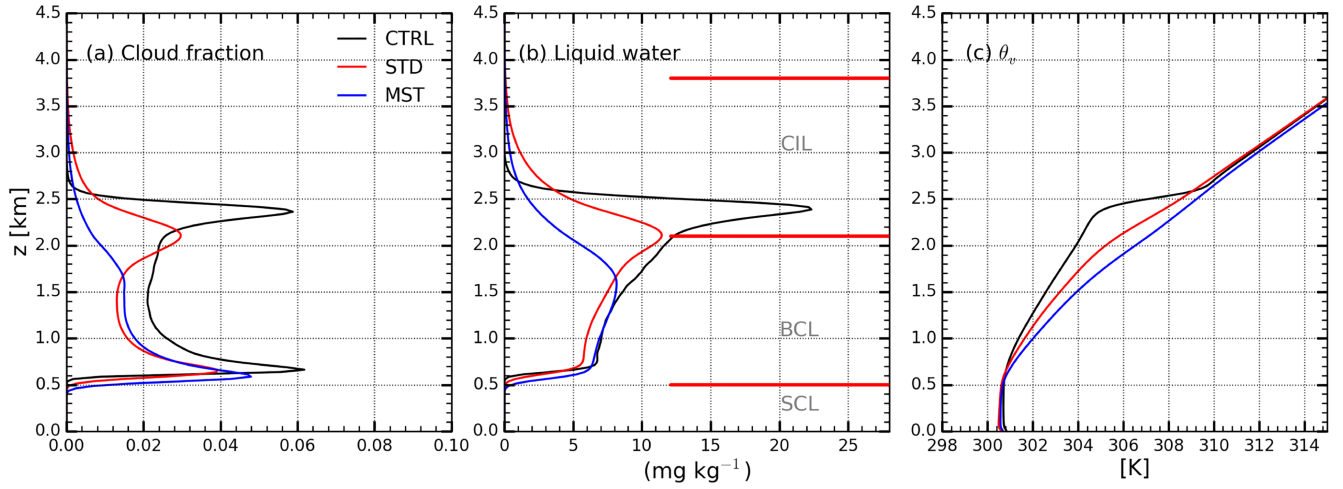
Figure 3. Mean profiles of (a) cloud fraction, (b) cloud liquid water, and (c) virtual potential temperature (θ_v). Profiles are averages over the entire domain from 30 to 35 hr of the simulation. Here SCL, BCL, and CIL correspond to the subcloud layer, the bulk cloud layer, and the cloud inversion layer, respectively. The layers are labeled based on the profiles for STD.

3.2.3. Budget Analyses

The contribution of the individual processes to the moisture variance budget is depicted in Figure 6. Small residuals indicate that the SGS terms are negligible. The variance budget for the control case is in good agreement with the results published by Heinze et al. (2015) for nonprecipitating shallow convection.

The gradient production term is the major source term, and dissipation is the main sink term for all the three cases. The turbulent transport term redistributes the moisture variance from regions of higher values toward regions of lower values. For the precipitating cases, microphysics is an additional sink term, especially near the upper part of the BCL and in the CIL. Therefore, we are interested in the difference for the microphysics between the two precipitating cases.

A detailed representation of the microphysical contributions to the $\overline{q_t'^2}$ budget is given in Figure 7 for the standard case. The microphysics term consists of three components:

$$\underbrace{2\overline{q_t'Q_{q_t}}}_{\text{microphysics}} = \underbrace{2\overline{q_t'Q_{q_t}^{\text{evap}}}}_{\text{evaporation}} + \underbrace{2\overline{q_t'Q_{q_t}^{\text{accr}}}}_{\text{accretion}} + \underbrace{2\overline{q_t'Q_{q_t}^{\text{auto}}}}_{\text{autoconversion}} .$$

Accretion is the dominant microphysical tendency term and is therefore the main sink in the $\overline{q_t'^2}$ budget. The evaporation and autoconversion terms are relatively small compared to the accretion term. The negative
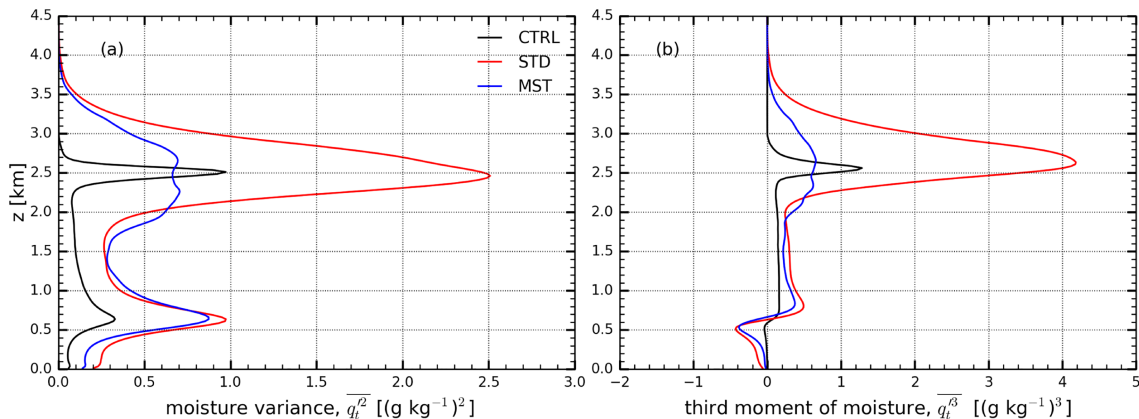
Figure 4. Mean profiles of (a) the moisture variance and (b) the TOM of moisture. Profiles are averages over the entire domain from 30 to 35 hr of the simulation.
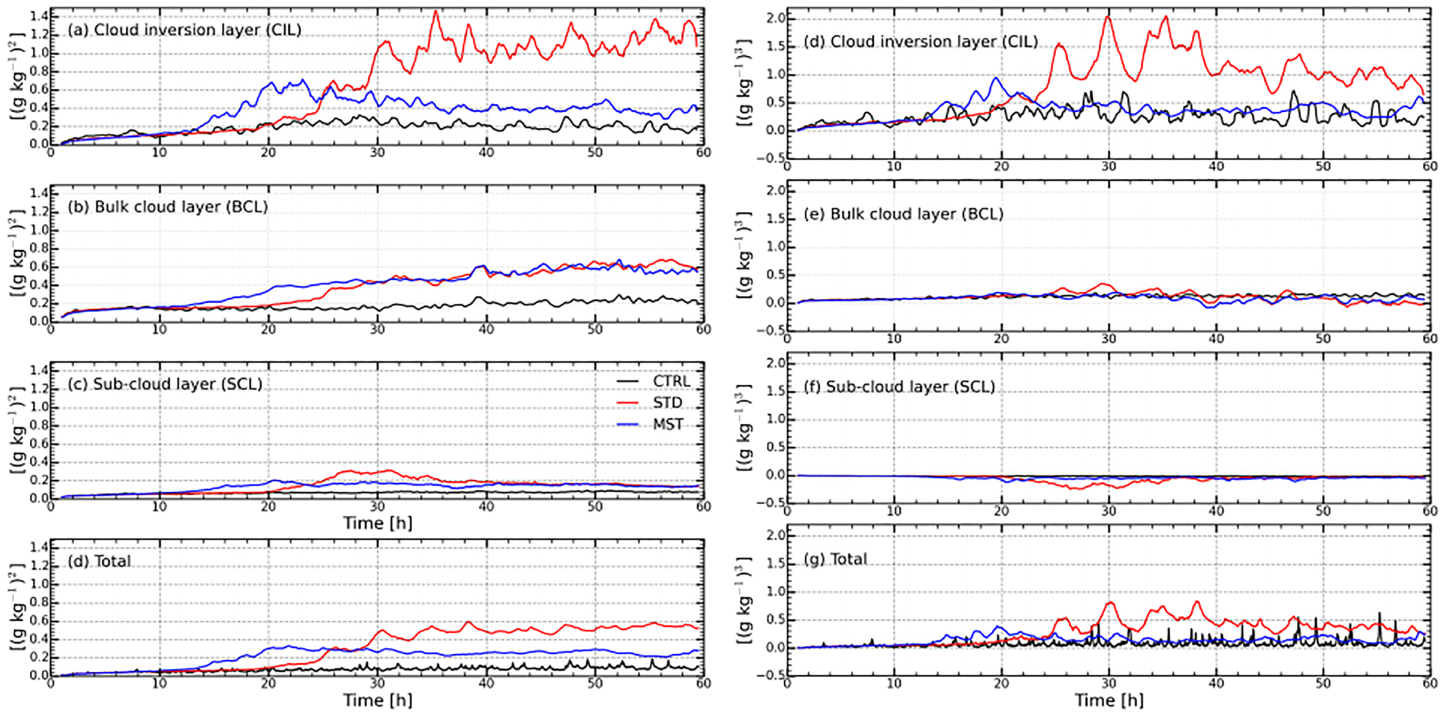
Figure 5. Time series of the moisture variance (left column) and the third-order moment of moisture (right column) in the three sublayers: (a, d) the cloud inversion layer, CIL; (b, e) the bulk cloud layer, BCL; (c, f) the subcloud layer, SCL; and (d,g) the entire ABL.

values of the evaporation term in the variance budget point to the presence of dry air in the subcloud layer ($\overline{2q_t'Q_{qt}} < 0$ and $Q_{qt} > 0$ thus $q_t' < 0$).

The budget of the TOM of moisture is shown in Figure 8. As for $\overline{q_t'^2}$, the residuals for the $\overline{q_t'^3}$ budget are small, implying that the budget analysis for $\overline{q_t'^3}$ is sufficiently accurate. For the three cases, dissipation is the main loss term over the whole region, while the gradient production of $\overline{q_t'^3}$ is the major source term in the cloud layer and above. The turbulent transport term redistributes $\overline{q_t'^3}$ from the source regions to the sink regions and is strongest in the SCL-BCL and BCL-CIL interfacial layers. As for the $\overline{q_t'^2}$ budget, the main differences between control and the precipitating simulations are the sink term due to microphysics and the less peaked
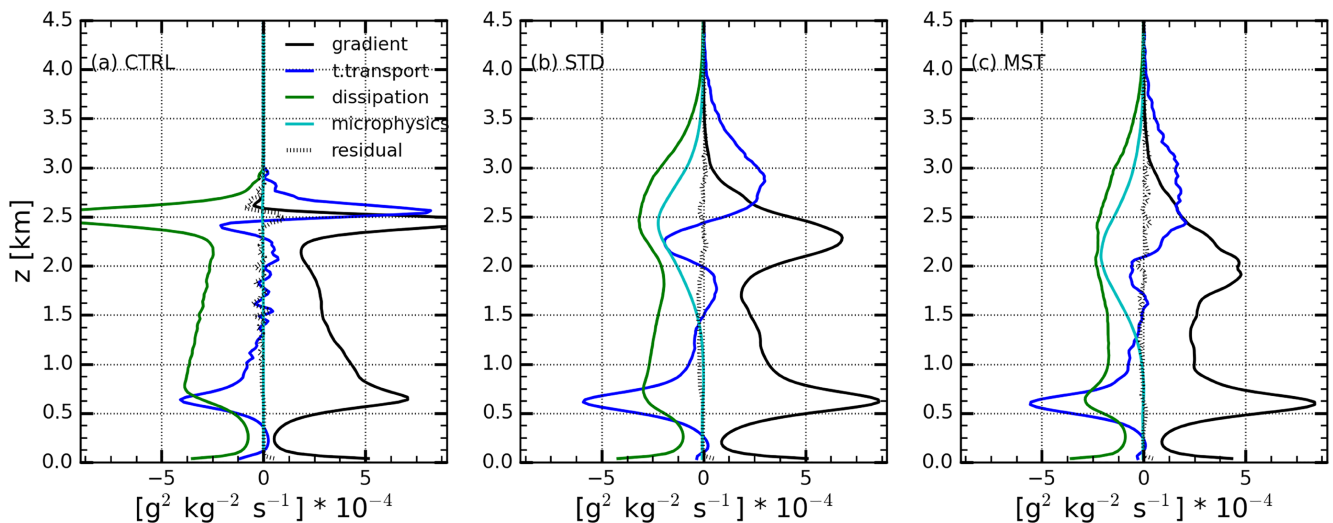
Figure 6. The moisture variance budget (average from 30 to 35 hr) for the three cases: (a) CTRL, (b) STD, and (c) MST. The budget terms are calculated according to equation (1).
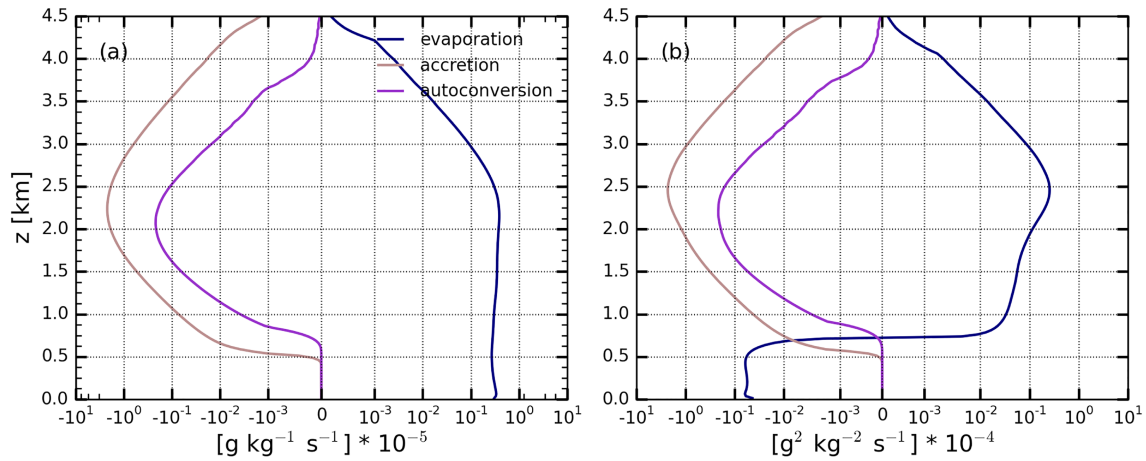
Figure 7. Profiles of (a) the microphysical tendencies $Q_{q_t}^x$ (evaporation, accretion, and autoconversion) and (b) the microphysical terms in the moisture variance budget ($\overline{2q_t'Q_{q_t}^x}$) for the standard case (STD) (average from 30 to 35 hr). Logarithmic scale is chosen for abscissa.

profiles at the BCL-CIL interface. Even though, the flux divergence is an additional term in the $\overline{q_t'^3}$ budget; its magnitude is small compared to Couvreux et al. (2007) and can be neglected in the present case. Overall, the vertical profiles of the budget terms for $\overline{q_t'^2}$ and $\overline{q_t'^3}$ are qualitatively similar but differ in magnitude. The vertical profiles and the temporal evolution (Figure 5) show that in this case the moisture variance is highly correlated with the TOM of moisture. Hence, in the remainder of the paper, we will proceed with the analyses of only the moisture variance, assuming that the mechanisms responsible for the generation of moisture variance are similar for the generation of the TOM of moisture.

3.2.4. Gradient Production Term
As shown in the budget analyses, the gradient production term is the main source term in the budget of the moisture variance. In order to explore the differences between the three cases, the individual contributions to the gradient production term are examined next. According to equation (1), the gradient production term is given by

$$\text{GPT} = -2\,\overline{q_t'w'}\frac{\partial \overline{q_t}}{\partial z}. \tag{6}$$

As can be seen, it depends on the product of the vertical moisture gradient and the vertical moisture flux.
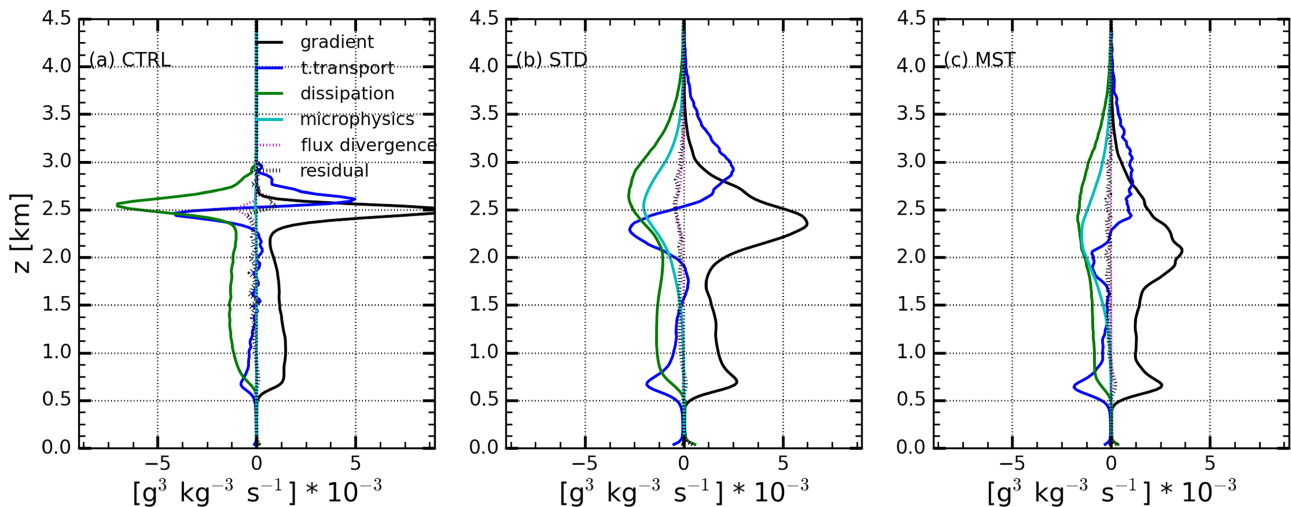
Figure 8. Profiles of the terms in the budget of the third-order moment (TOM) of moisture (30 to 35 hr): (a) CTRL, (b) STD, and (c) MST.

In our case, the vertical moisture flux and the vertical moisture gradient are linked, because the vertical moisture flux is mostly countergradient in shallow convection (see e.g.; Bastak Duran et al., 2018). Thus, the vertical moisture flux, if present, reduces the vertical moisture gradient. On the other hand, if the vertical moisture gradient is very sharp, it is an indication of a negligible moisture flux across that region, which is typically caused by stable stratification. Since both components influence the resulting gradient production term, their interaction is critical for the generation of moisture variance.

The left column in Figure 10 shows the moisture flux, the moisture gradient, the resulting gradient production term, and the moisture variance for all three cases.

The biggest differences between the control case and the precipitating cases are around the BCL-CIL transition (near the region where q_l reaches its maximum; see Figure 3). The control case has a larger vertical moisture flux and a sharper vertical moisture gradient at this transition than the precipitating cases. At the same time, the precipitating cases have a vertically extended CIL, where both the moisture flux and the moisture gradient are nonnegligible. Among the precipitating cases, the moisture fluxes are similar, but the moisture gradient at the BCL-CIL transition is larger for the standard case, resulting in a larger gradient production term. The gradient production term generates moisture variance in the extended CIL in the precipitating cases, while it is negligible for the control case at the same vertical levels.

Overall, more moisture variance is generated for the precipitating cases than for the control case (with significantly higher values for the moist case). The differences in moisture variance between the cases do not completely correspond to the differences in the gradient production term at the given time, indicating that the vertical profiles of moisture variance are a result of a longer temporal evolution.

The differences in moisture variance between the three cases are caused by two main process, the continuous moistening of the boundary layer via the surface moisture flux and the penetration of the BCL-CIL transition via active precipitating convection. In the initial regime, the magnitude of the moisture gradient (the moisture gradient is negative) at the BCL-CIL interface grows for all three cases due to the surface moisture flux (see Figure 9). When there is sufficient moisture, respectively, latent heat release, near the BCL-CIL interface, convective plumes begin to precipitate and penetrate the BCL-CIL interface. This marks the beginning of the transition regime. This regime is never reached for the control case; it is reached earlier for the moist case, due to the higher initial moisture in the boundary layer.

The active penetrating convection transports moisture across the BCL-CIL interface. This causes the reduction of the moisture gradient at the BCL-CIL transition and the formation of a new moisture gradient above the former CIL, thus extending the vertical extent of the CIL. In the process, moisture variance is generated via the gradient production term in the CIL, because both the moisture gradient and the moisture flux have large magnitudes. When the moisture gain due to the surface flux and the moisture loss due to the transport across the BCL-CIL interface balance each other in the BCL, the transition regime ends, and the quasi-steady is reached. Because the standard case has a drier initial boundary layer, the equilibrium moisture gradient is larger, and the accumulation of moisture variance in the BCL lasts longer. Hence, more moisture variance is generated for the standard case in the transition regime (see Figure 5). The control case does not have a transition regime, where additional moisture variance could be generated; therefore, the moisture variance in the control case is smaller than in the precipitating cases.

3.2.5. Conditional Sampling

While the budget analysis is a useful tool for understanding the moisture variance, useful information may be lost due to the domain averaging, such as the contribution of different areas and convective activity to the budget terms. In order to investigate the importance of convective regions, a conditional sampling of the LES data is performed (see section 2.2). Here, we focus only on the main source term in the moisture variance budget, the gradient production term, and its components: the turbulent moisture flux $\overline{q_t'w'}$ and the moisture gradient $\partial\overline{q_t}/\partial z$.

Profiles of the three terms for the entire domain, the CA region, and the NA region are presented in Figure 10. It can be seen that the moisture flux is larger and reaches higher altitudes for the precipitating cases in the CA region, while it is of comparable magnitudes for all three cases in the NA region. This confirms the assumption that the intense moisture flux for the precipitating cases is a consequence of the increased convective activity associated with the precipitation. In the domain average, the differences in the moisture flux between the three experiments are less pronounced than in the CA region, because the larger values of
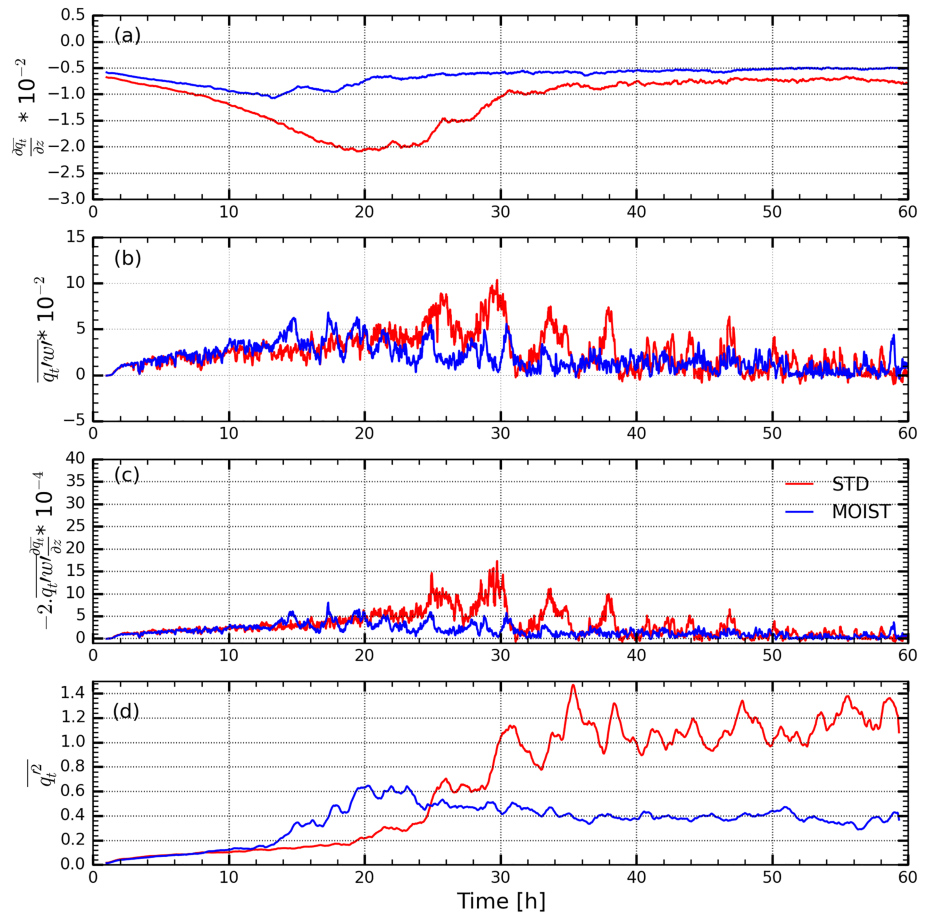
Figure 9. Time evolution of (a) the maximum vertical gradient of the mean moisture at the BCL-CIL interface, (b) the vertical moisture flux, (c) the gradient production term of moisture variance, and (d) the moisture variance. The latter three quantities are vertically averaged over the cloud inversion layer (CIL).

the moisture flux in the CA region for the precipitating cases are compensated by a smaller size of the CA region (7% for the precipitating cases vs. 17% for the control case).

For each case, the profiles of the moisture gradient are similar for both the CA and the NA regions: Their magnitudes are smaller within the SCL, the BCL and the CIL and are larger at the layer interfaces. The gradients are less sharp and extend to the higher levels for the precipitating cases.

Because there are no big differences among the three cases in the moisture gradients, the main factor that causes the differences among the three cases in the gradient production term is the moisture flux in the CA region. As for the moisture flux, the differences in the gradient production term are smaller in the domain average than in the CA region.

As discussed in section 3.2.4, the differences in the moisture variance between the cases are created in the transition regime via the gradient production term. In the CA region, the differences in the moisture variances roughly correspond to the magnitude of the gradient production term, but surprisingly, they are also significantly different in the NA region (especially in the CIL). This indicates that there are additional terms contributing to the increase of moisture variance in the NA region for the precipitating cases. The horizontal transport between the CA region (with a high moisture variance) and the NA region could contribute to an increase of the moisture variance in the NA region. We will study this potential link between the moisture variance and the dynamics in the next subsection.

A second possibility is that the moisture variance was generated in this region at an earlier time, when it was CA. To demonstrate this, a conditional budget analysis, including horizontal terms, for the standard case is presented in Figure 11. We can see that indeed, the moisture variance increase cannot be attributed
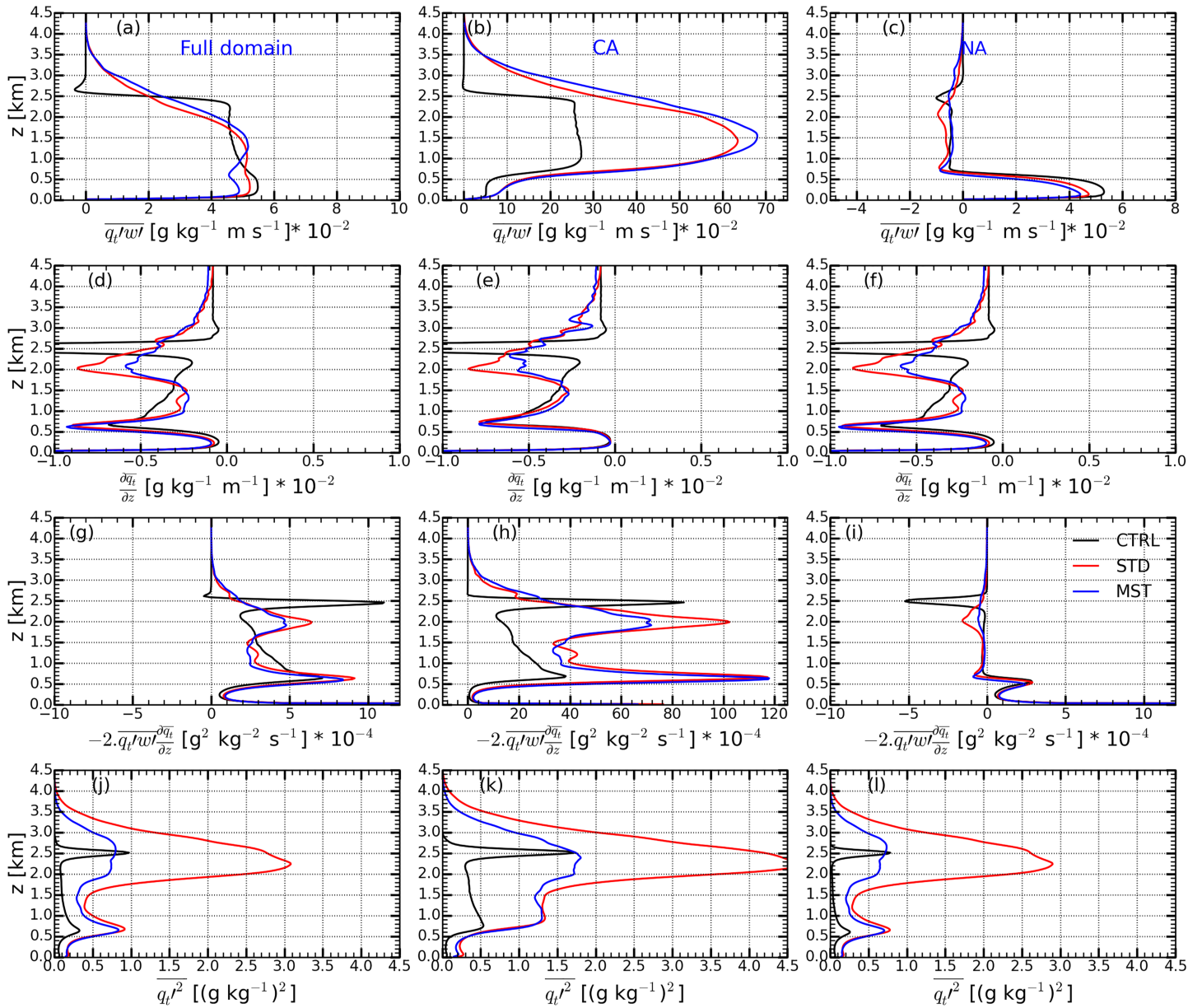
Figure 10. Profiles of the vertical moisture flux (a–c), the vertical gradient of the mean moisture (d–f), the gradient production term (g–i), and the moisture variance (j–l) (averages from 30 to 35 hr). The left column represents the domain average, the middle column corresponds to spatial average from the cloud active (CA) area, and the right column shows the spatial average from the nonactive (NA) area.

only to the horizontal terms. The moisture variance even decreases for the NA region in the CIL despite the positive contribution of the horizontal terms (negative tendency term). This confirms the assumption that there was a previous accumulation of moisture variance in NA, and since it became an inactive region, the moisture variance gradually decreases in the CIL.

3.3. Moisture Variance and Flow Dynamics

To address the link between the moisture variance and the flow dynamics, we examine the spatial distribution of the three quantities that contribute to the domain averaged moisture variance and the gradient production term: $q_t'^2$, q_t', and $w' q_t' \frac{\partial q_t}{\partial z}$. For the sake of brevity, we analyze the differences only between the control case and the standard precipitating case, where the standard case is representative for both precipitating cases.
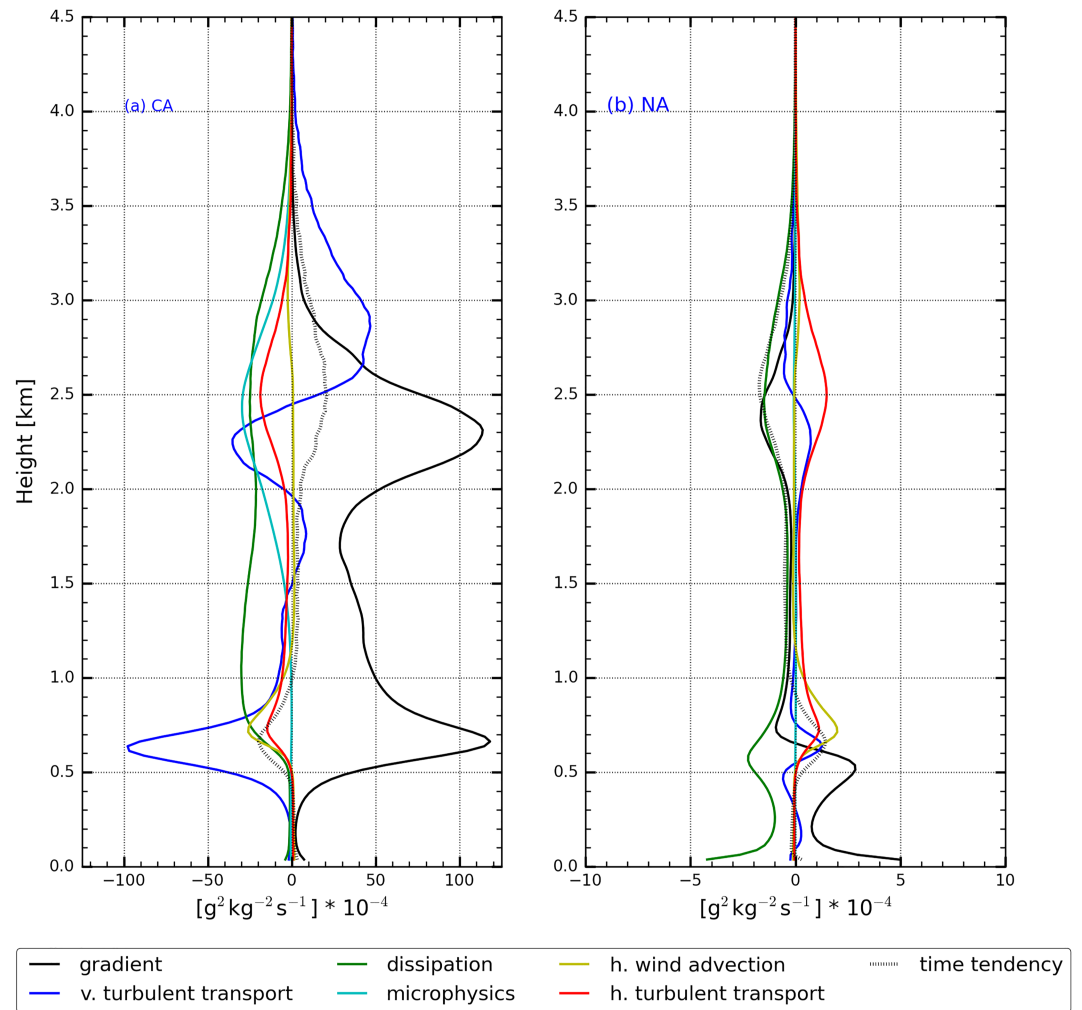
Figure 11. Profiles of the term from the moisture variance budget in the (a) CA and (b) NA region for the standard case (STD; averages from 30 to 35 hr). The budget terms are calculated according to equation (3). Note the different scales of the *x* axis in the two panels.
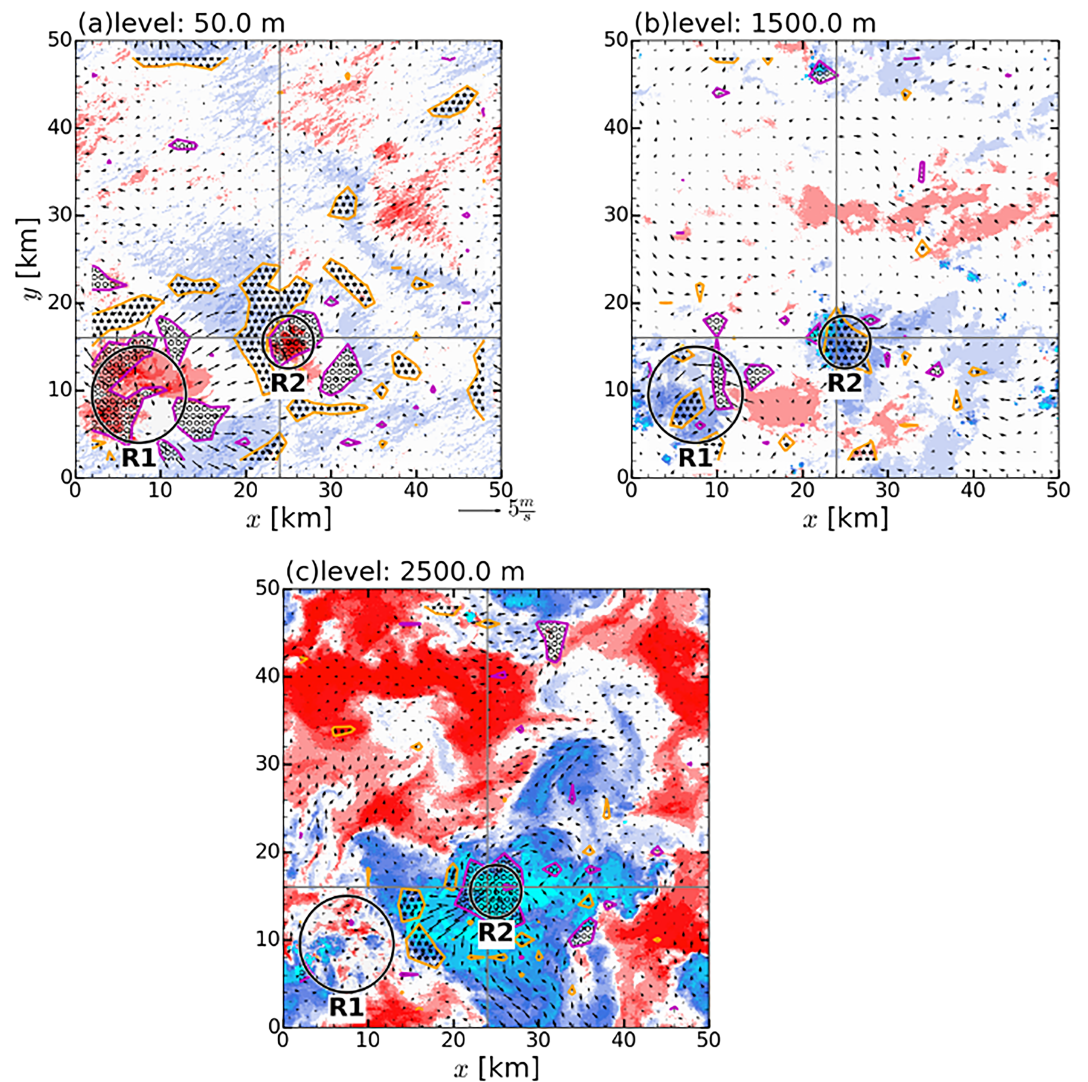
Figure 12 depicts the horizontal cross section of $q_t'^2$ after 35 hr of integration at three different heights: 50, 1,500, and 2,500 m, which represent the SCL, BCL, and CIL, respectively. Note, that by averaging $q_t'^2$ over the whole domain, we acquire the moisture variance; hence, the snapshot shows how the individual regions contribute to the moisture variance. In the SCL, the high values of $q_t'^2$ are concentrated in several regions for the standard case. The two strongest ones are marked with circles in the figure, and we will refer to them as R1 and R2. A similar pattern of $q_t'^2$ distribution is visible in BCL. In CIL, we can observe that the region of large values of $q_t'^2$ is centered approximately over R2, but it is much larger.

Moisture variance can be caused either by moist or dry moisture fluctuations, to distinguish between the two possibilities; the moisture fluctuations q_t' are displayed in Figure 13 for the standard case. The figure also shows instantaneous wind vectors (averaged over 2 km × 2 km regions) and the corresponding horizontal convergence and divergence of the smoothed horizontal wind field.

Within the SCL, the Regions R1 and R2 are mainly composed of dry air patches having negative moisture perturbations. The horizontal wind field within R1 and R2 shows a net divergence and the wind vectors clearly display outward flow from R1 and R2. Some patches of convergence are also visible at the edges of these regions of divergence, which may lead to subsequent development of convection. This seems like a typical characteristic of convective cold pools with divergence in the cold pool center where downdraft air spreads out and convergence at the leading edge of the cold pool (Drager, 2016). The downdraft can be seen
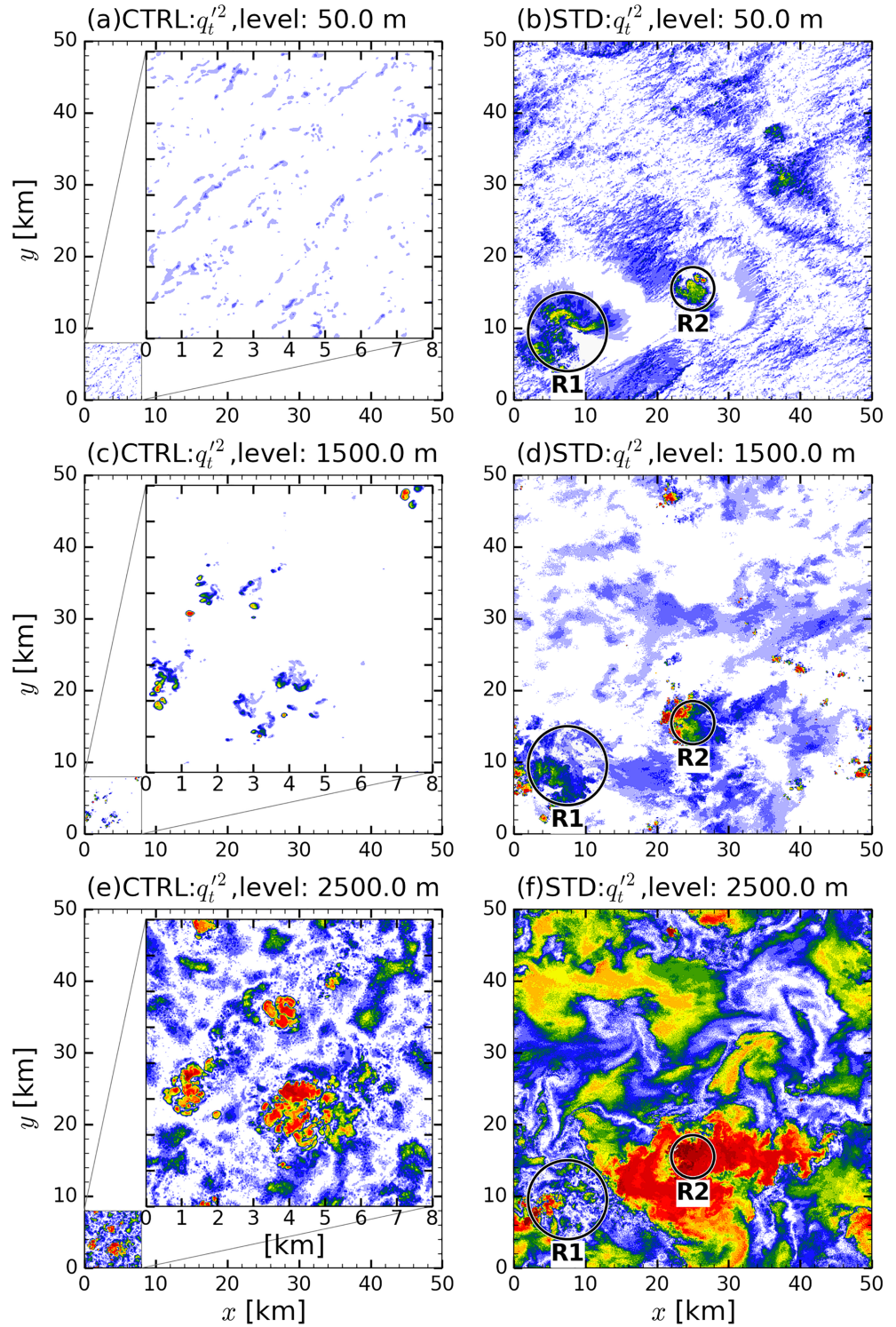
Figure 12. Horizontal cross sections of $q_t'^2$ [(g kg^{-1})^2] at 50, 1,500, and 2,500 m, at simulation time 35 hr. The control simulation (CTRL) is shown over its 8 × 8 km domain in panels (a), (c), (e) and zoomed out for comparison with the standard case (STD) in (b), (d), (f). R1 and R2 demark the two regions with the strongest moisture fluctuations in the subcloud layer.

Figure 13. Horizontal cross section of moisture perturbations q'_t (g kg^{-1}) at (a) 50, (b) 1,500, and (c) 2,500 m, respectively, at simulation time 35 hr for the standard case. R1 and R2 denote the two regions of interest introduced in Figure 12. The arrows denote anomalies of the horizontal wind. The convergence and divergence of the horizontal wind field is represented using orange and magenta contours, respectively. The convergence zone is additionally filled with star hatches and the divergence zone with open circles. The gray lines represent the location of xz and yz cross sections shown in Figure 16.

in the center of R2 in Figure 14a. However, the convective cell in R1 appears to be in a more mature stage, where the downdraft is almost depleted and only the divergent flow is still visible.

Studies have shown that the cold pool-induced subcloud moisture fields are tightly coupled to the organization of clouds and convection (Schlemmer & Hohenegger, 2016; Seifert & Heus, 2013). Depending on the rate of precipitation, a downdraft can either moisten or dry an area within the SCL (Schlemmer & Hohenegger, 2016). For the RICO simulation, Seifert and Heus (2013) have documented pronounced dry cores associated with the cold pools in the subcloud layer, which agrees with our findings.

In the BCL, in contrast to the SCL, the R1 and R2 regions contain convective moist updrafts accompanied by convergent flow.

In the CIL, a smaller region with moist fluctuations that could correspond to R1 is located to the southwest of R1. The Region R2 is a center of a larger region with moist fluctuations and strong divergent flow. This
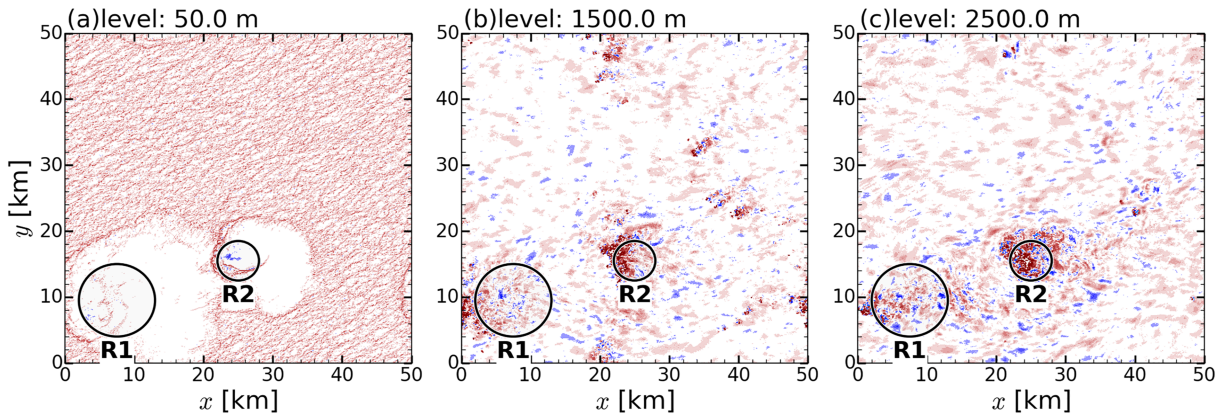
Figure 14. Horizontal cross section of vertical velocity perturbation w' (m s^{-1}) at (a) 50, (b) 1,500, and (c) 2,500 m, respectively, at simulation time 35 hr. R1 and R2 are the main regions of interest.

and the fact that moisture variance is generated mainly inside R2 (see horizontal distribution of the gradient production term source term in Figure 15) indicates that there is an anvil-like horizontal spreading of moisture variance from R2 to the surrounding area.

To complement the above analysis, Figure 16 shows vertical cross sections of $q_t'^2$ and q_t' that cut through R2 at $y = 16$ km and $x = 24$ km, respectively, along with the circulation (wind vectors) within the corresponding cross section. The figures reveal that the circulation in the convective cell is more complicated than expected from the horizontal cross sections. A shallow region of divergence (violet line) and dry air (red shading) linked to a downdraft (arrows pointing down) can be seen in the SCL, which neighbors a much deeper convergence region (orange line) linked to an updraft (arrows pointing up). Moist air (blue shading) associated with this convergence zone extends vertically as a narrow, weak updraft from the SCL, intensifies in the BCL, and diverges finally into a wider area in the CIL. Hence, the flow fields show a region of convergence in the BCL, accompanied by corresponding region of divergence in the SCL and the CIL.

In summary, the main increase of moisture variance is caused by the gradient production term. The term is significant if both the vertical gradient of moisture and the vertical moisture flux are nonnegligible (see equation (6)). While the mean moisture content decreases with the height in the entire boundary layer (with stronger decrease near the interfaces of the three distinct layers; see Figure 10), the vertical moisture flux is strong only in the moist/dry downdrafts or updrafts. As we can see from above analysis, these vertical fluxes are located in CA regions, specifically in the shallow dry downdrafts in the SCL and in the
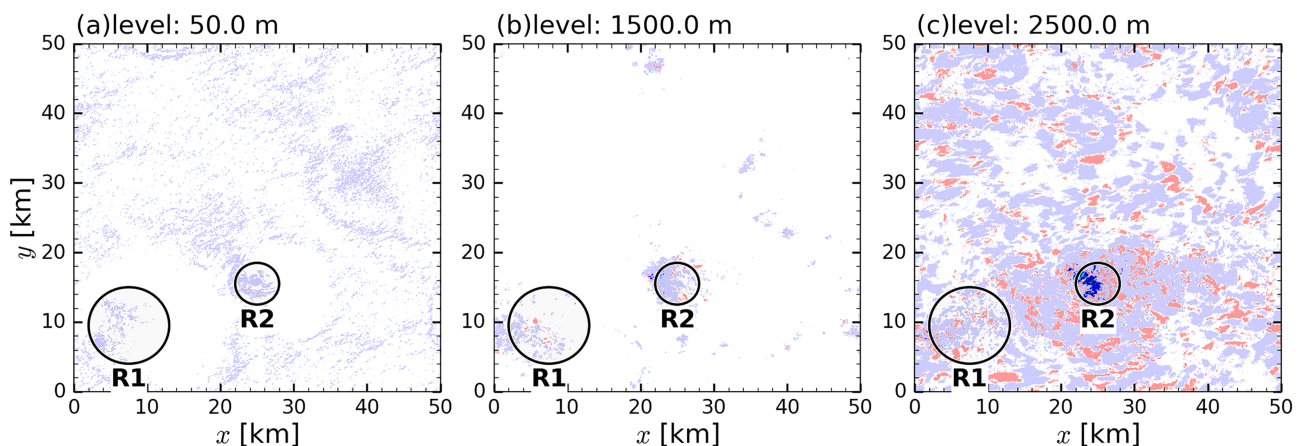
Figure 15. As Figure 14 but for the term $q_t' w' \overline{\frac{\partial q_t}{\partial z}}$ (g kg^{-2} m s^{-1}).
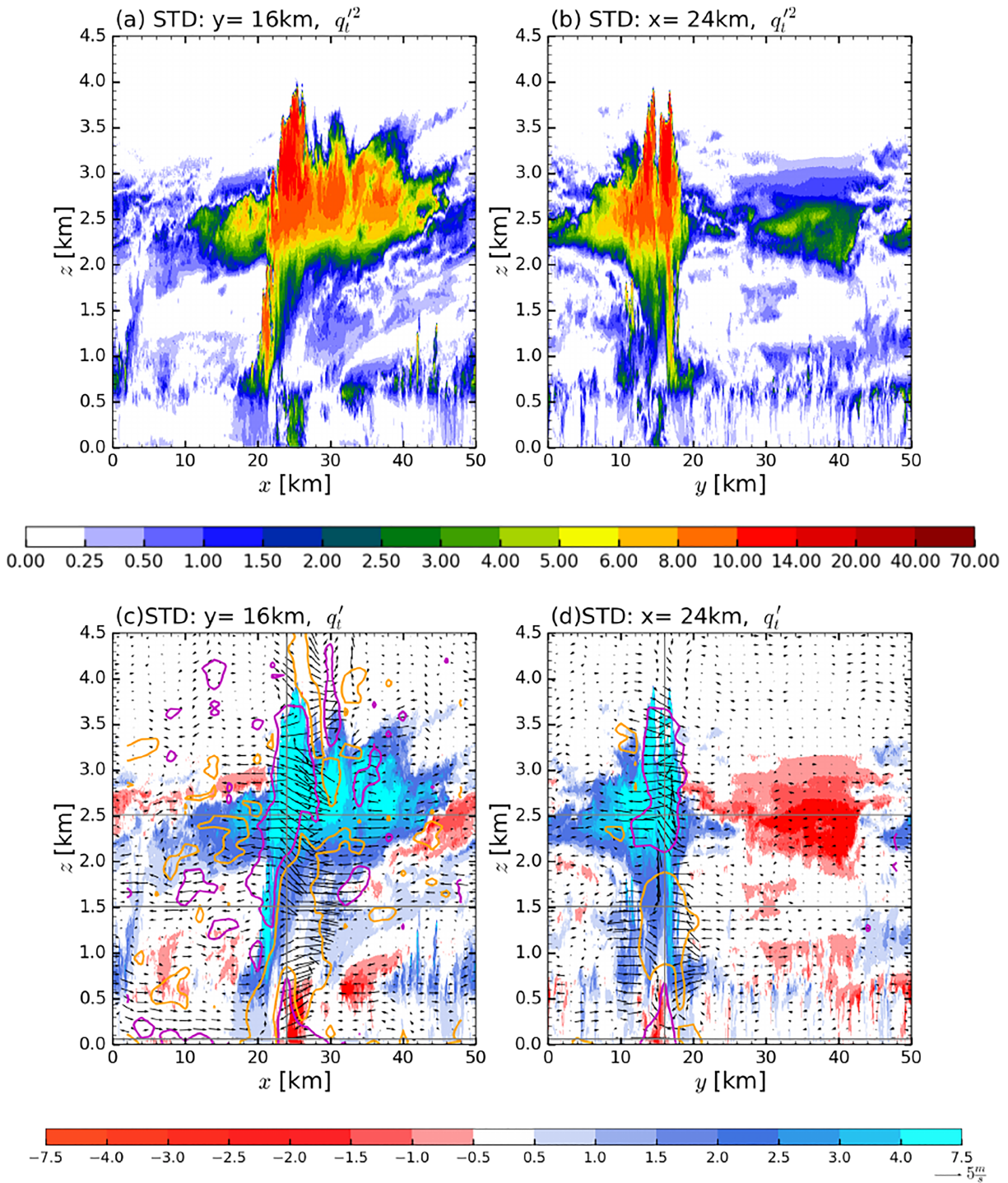
Figure 16. Vertical xz cross section at $y = 16$ km and yz cross section at $x = 24$ km of $q_t'^2$ [(g kg^{-1})^2] (a,b), and q_t' [g kg^{-1}] (c,d) at simulation time 35 hr. The vectors denote the wind anomalies in the corresponding cross section. The convergence and divergence of the horizontal wind field are represented using orange and magenta contours, respectively. The gray lines are the levels representing 50, 1,500, and 2,500 m.

Table 2
Key Characteristics of the Precipitating and Nonprecipitating Simulations

Characteristic	Nonprecipitating shallow convection	Precipitating shallow convection
Organization	Random or small scale	Mesoscale arcs
Precipitation	None	Moderate (1 mm day^{-1})
Cloud cover	Higher ($\sim$40%)	Lower ($\sim$20%)
Liquid water path	Higher ($\sim$30 g m^{-2})	Lower ($\sim$10 g m^{-2})
Coupling to free atmosphere	Lower	Higher
Cloud active area	17%	7%
Bulk cloud layer	Deeper	More shallow
Cloud inversion layer	Shallow	Deep
Budget of moisture variance	Lower ($\sim$0.1 [g kg^{-1}]^2))	Higher ($\sim$0.2–0.5 [g kg^{-1}]^2)
Moisture variance	MP ~ 0	MP < 0
Budget of TOM	MP ~ 0	MP < 0

Note. Here "MP stands for microphysics.

moist updrafts in the CIL. The divergent flow in these regions then further transports the generated moisture variance horizontally. As expected, this transport contributes to an increase of moisture variance in the neighboring NA regions.

The microphysical processes directly decrease moisture variance (see budget analysis in Figure 6). However, microphysics is a principal driver of the processes in the active precipitating convection; hence, microphysics indirectly increases the moisture variance via the dynamics.

4. Summary and Conclusion

A detailed analysis of moisture variance in a precipitating CBL has been performed in this study, in order to understand the link between the moisture variance (and the TOM of moisture) and the processes that are connected to cloud organization and precipitation. An improved understanding of this link offers a possibility for the development of parameterizations of cloud organization in numerical weather prediction and climate models.

Three idealized LES runs based on the RICO experiment were performed using MicroHH. Two of the simulations (the standard case and the moist case) are carried out on a large domain covering an area of 50 $\times$ 50 km, thus allowing the formation of precipitation and mesoscale organization of clouds. An additional control simulation is conducted over a small domain (with an otherwise identical setup as for the standard case) in order to prevent the formation of precipitation and mesoscale organization.

The results show that precipitation and the associated cloud organization lead to the increased generation of HOMs of moisture (moisture variance and third-order moment of moisture) compared to the nonprecipitating case. This increase in the precipitating cases is mainly caused by the local penetration of intensified moist convection into dry and stable layers above the original cloud layer. The transport of air from the BCL into the expanding CIL changes the vertical structure of the boundary layer and significantly contributes to the increased generation of HOMs of moisture via the gradient production term, which depends both on the moisture gradient and the moisture flux. In contrast, the direct effect of the microphysics is to decrease the generation of HOMs of moisture, but this effect is not dominant. Turbulent transport also plays a non-negligible role and becomes significant in the interface regions between the layers. Table 2 summarizes the main differences between the precipitating and nonprecipitating cases as inferred from these results.

Three different regimes in the evolution of the moisture variance were identified: an initial regime, prior to the onset of precipitation; a transition regime, starting with the onset of precipitation; and a quasi-steady state regime. The column-integrated moisture variance is increased during the transition regime (see Figure 5) via the gradient production term mainly in the CIL. This increase in moisture variance is caused mainly by the precipitation-induced increase in convective activity, which in turn is enabled through the mesoscale organization of the clouds. The precipitating convective plumes are able to penetrate deeper into the CIL. In

this process, moisture variance is generated via the gradient production term in the CIL, since both components of the gradient production term, the moisture gradient, and the moisture flux are large in this region. The moisture variance in the control case is smaller, because the control case does not reach the precipitating transition regime due to a lack of cloud organization in its smaller domain. Comparing the precipitating cases, more moisture variance is generated in the standard case. While both precipitating cases have similar moisture flux profiles, once precipitate starts, the vertical gradients of moisture are sharper in the standard case. This is the result of the longer accumulation period required in the standard case to initiate precipitation. The increased moisture variance is horizontally transported to adjacent NA regions and remains in the area when the region becomes NA. Hence, the moisture variance is also increased in the NA regions.

Further analysis of horizontal and vertical cross sections of the simulated flow confirms that the precipitation-induced updrafts and downdrafts are the main mechanism for the generation of increased moisture variance. The variance increase is linked to a shallow dry downdraft region with horizontal divergence in the SCL, a weak moist updraft region with horizontal convergence in the BCL, and finally a wider area of horizontal divergence in the CIL. Though evaporation of rain does not contribute directly to the moisture variance, evaporative cooling of rain below the cloud base promotes the downdrafts. These negatively buoyant air parcels induce divergent flow near the surface, collide with the neighboring cells at cold pool boundaries, and induce secondary moist updrafts. The moist updrafts in the cloud layer can be attributed to updrafts preconditioned by earlier convection and to secondary convection from the edges of the cold pools, but it will be difficult to disentangle the two cases.

The impact of precipitation on the generation of moisture variance is indirect, because of the small-scale, short-lived, and nonsimultaneous nature of the processes. Thus, it is not represented directly through the microphysics term in the Reynolds-averaged equations. This makes the system very complex and challenging from the parametrization point of view. Nevertheless, based on these results, an empirical framework for the parameterization of mesoscale cloud organization could be developed. Such a framework would need to entail the indirect influence of the microphysics on the moisture variance via a communication between the parametrization of microphysics and the explicit or implicit (depending on the scheme) parametrization of HOMs, preferably via the gradient production term. In addition, a parametrization of subgrid scale cloud organization should be considered. Development of a new parametrization is beyond the scope of our paper, and we leave it for further studies.

References

Bastak Duran, I., Geleyn, J.-F., Vana, F., Schmidli, J., & Brozkova, R. (2018). A turbulence scheme with two prognostic turbulence energies. *Journal of the Atmospheric Sciences*, *75*(10), 3381–3402. https://doi.org/10.1175/JAS-D-18-0026.1

Bastak Duran, I., Theethai Jacob, A., Schmidli, J., & Seifert, A. (2019). Data for understanding the moisture variance in precipitating shallow cumulus convection [Data set]. *Zenodo*. http://doi.org/10.5281/zenodo.3472616

Bodine, D., Heinselman, P. L., Choeng, B. L., Palmer, R. D., & Michaud, D. (2010). A case study on the impact of moisture variability on convection initiation using radar refractivity retrievals. *Journal of Applied Meteorology and Climatology*, *49*(8), 1766–1778. https://doi.org/10.1175/2010JAMC2360.1

Bogenschutz, P. A., & Krueger, S. K. (2013). A simplified PDF parameterization of subgrid-scale clouds and turbulence for cloud-resolving models. *Journal of Advances in Modeling Earth Systems*, *5*, 195–211. https://doi.org/10.1002/jame.20018

Bretherton, C. S., & Blossey, P. N. (2017). Understanding mesoscale aggregation of shallow cumulus convection using large-eddy simulation. *Journal of Advances in Modeling Earth Systems*, *9*, 2798–2821. https://doi.org/10.1002/2017MS000981

Cheng, A., & Xu, K. M. (2015). Improved low-cloud simulation from the community atmosphere model with an advanced third-order turbulence closure. *Journal of Climate*, *28*(14), 5737–5762. https://doi.org/10.1175/JCLI-D-14-00776.1

Couvreux, F., Guichard, F., Masson, V., & Redelsperger, J. L. (2007). Negative water vapour skewness and dry tongues in the convective boundary layer: Observations and large-eddy simulation budget analysis. *Boundary-Layer Meteorology*, *123*(2), 269–294. https://doi.org/10.1007/s10546-006-9140-y

Couvreux, F., Redelsperger, J.-L., Guichard, F., Kiemle, C., Masson, V., Lafore, J. P., & Lamant, C. (2005). Water-vapour variability within a convective boundary-layer assessed by large-eddy simulations and IHOP_2002 observations. *Quarterly Journal of the Royal Meteorological Society*, *131*(611), 2665–2693. https://doi.org/10.1256/qj.04.167

Cuijpers, J., Duynkerke, P., & Nieuwstadt, F. (1996). Analyses of variance and flux budgets in cumulus-topped boundary layers. *Atmospheric Research*, *40*(2-4), 307–337. https://doi.org/10.1016/0169-8095(95)00033-X

Deardorff, J. W. (1974). Three-dimensional numerical study of turbulence in an entraining mixed layer. *Boundary-Layer Meteorology*, *7*(2), 199–226. https://doi.org/10.1007/BF00227913

Drager, A. J. (2016). *Convective cold pools: Characterisation and soil moisture dependence.* Master Thesis, (p. 97).

Golaz, J., Larson, V. E., & Cotton, W. R. (2001). A PDF-based model for boundary layer clouds. Part I: Method and model description. *Journal of the Atmospheric Sciences*, *59*, 3540–3551.

Griffin, B. M., & Larson, V. E. (2016). Parameterizing microphysical effects on variances and covariances of moisture and heat content using a multivariate probability density function: A study with CLUBB (tag MVCS). *Geoscientific Model Development*, *9*(11), 4273–4295. https://doi.org/10.5194/gmd-9-4273-2016

Heinze, R., Mironov, D., & Raasch, S. (2015). Second-moment budgets in cloud topped boundary layers: A large-eddy simulation study. *Journal of Advances in Modeling Earth Systems*, *43*, 28802900. https://doi.org/10.1002/2014MS000376

Lappen, C., & Randall, D. A. (2001). Toward a unified parameterization of the boundary layer and moist convection. Part I: A new type of mass-flux model. *Journal of the Atmospheric Sciences*, *58*(15), 2021–2036. https://doi.org/10.1175/1520-0469(2001)058<2021:TAUPOT> 2.0.CO;2

Larson, V. E., & Golaz, J. C. (2005). Using probability density functions to derive consistent closure relationships among higher-order moments. *Monthly Weather Review*, *133*(4), 1023–1042. https://doi.org/10.1175/MWR2902.1

Lilly, D. K. (1968). Models of cloud-topped mixed layers under a strong inversion. *Quart. J. Roy. Meteor. Soc.*, *94*(401), 292–309. https://doi. org/10.1002/qj.49709440106

Mahrt, L. (1991). Boundary-layer moist regimes. *Quarterly Journal of the Royal Meteorological Society*, *117*, 151–176.

Matheou, G., Chung, D., Nuijens, L., Stevens, B., & Teixeira, J. (2011). On the fidelity of large-eddy simulation of shallow precipitating cumulus convection. *Monthly Weather Review*, *139*(9), 2918–2939. https://doi.org/10.1175/2011MWR3599.1

Mellado, J. P., Puchea, M., & van Heerwaarden, C. C. (2017). Moisture statistics in free convective boundary layers growing into linearly stratified atmospheres. *Quarterly Journal of the Royal Meteorological Society*, *143*(707), 2403–2419. https://doi.org/10.1002/qj.3095

Mellor, G. L., & Yamada, T. (1974). A hierarchy of turbulence closure models for planetary boundary layers. *Journal of the Atmospheric Sciences*, *31*(7), 1791–1806. https://doi.org/10.1175/1520-0469(1974)031<1791:AHOTCM>2.0.CO;2

Mellor, G. L., & Yamada, T. (1982). Development of a turbulence closure model for geophysical fluid problems. *Reviews of Geophysics*, *20*(4), 851–875. Retrieved from. https://doi.org/10.1029/RG020i004p00851

Moeng, C. H., & Wyngaard, J. C. (1989). Evaluation of turbulent transport and dissipation closures in second -order modeling. *Journal of the Atmospheric Sciences*, *46*(14), 2311–2330. https://doi.org/10.1175/1520-0469(1989)046<2311:EOTTAD>2.0.CO;2

Neggers, R. A. J., Stevens, B., & Neelin, J. D. (2007). Variance scaling in shallow-cumulus-topped mixed layers. *Quarterly Journal of the Royal Meteorological Society*, *133*(628), 1629–1641. https://doi.org/10.1002/qj.105

Nuijens, L., Stevens, B., & Siebesma, A. (2003). The environment of precipitating shallow cumulus convection. *Journal of the Atmospheric Sciences*, *66*(7), 1962–1979. https://doi.org/10.1175/2008JAS2841.1

Rauber, R. M., Stevens, B., III, H. T. O., Knight, C., Albrecht, B. A., Blyth, A. M., et al. (2007). Rain in shallow cumulus over the ocean: The RICO campaign. *Bull. Amer. Meteor. Soc*, *88*, 1912–1928.

Roode, S. R. D., Duynkerke, P., & Jonker, H. M. M. (2004). Large-eddy simulation: How large is large enough? *Journal of the Atmospheric Sciences*, *64*, 403–421.

Schemann, V., & Seifert, A. (2017). A budget analysis of scalar variances in precipitating shallow cumulus convection. *Boundary-Layer Meteorology*, *163*(3), 357–373. https://doi.org/10.1007/s10546-016-0230-1

Schlemmer, L., & Hohenegger, C. (2016). Modifications of the atmospheric moisture field as a result of cold-pool dynamics. *Quarterly Journal of the Royal Meteorological Society*, *142*(694), 30–42. https://doi.org/10.1002/qj.2625

Seifert, A., & Beheng, K. D. (2001). A double-moment parameterization for simulating autoconversion, accretion and selfcollection. *Atmospheric Research*, *59-60*, 265–281. https://doi.org/10.1016/S0169-8095(01)00126-0

Seifert, A., & Heus, T. (2013). Large-eddy simulation of organized precipitating trade wind cumulus clouds. *Atmospheric Chemistry and Physics*, *13*(11), 5631–5645. https://doi.org/10.5194/acp-13-5631-2013

Seifert, A., Heus, T., Pincus, R., & Stevens, B. (2015). Large-eddy simulation of the transient and near-equilibrium behavior of precipitating shallow convection. *Journal of Advances in Modeling Earth Systems*, *7*, 1918–1937. https://doi.org/10.1002/2015MS000489

Short, D., & Nakamura, K. (2000). Trmm radar observations of shallow precipitation over the tropical oceans. *Journal of Climate*, *13*, 4107–4124.

Siebesma, A. P., Bretherton, C., Brown, A., Chlond, A., Cuxart, J., Duynkerke, P., et al. (2003). A large eddy simulation inter-comparison study of shallow cumulus convection. *Journal of the Atmospheric Sciences*, *60*(10), 1201–1219. https://doi.org/10.1142/ S0578563408001843

Snodgrass, E. R., Girolamo, L. D., & Rauber, R. M. (2009). Precipitation characteristics of trade wind clouds during RICO derived from radar, satellite, and aircraft measurements. *Journal of Applied Meteorolgy*, *48*, 464–483.

Stull, R. B. (1988). *An introduction to boundary layer meteorology*, (Vol. 17). P.O. Box 17, 3300 AA Dordrecht, The Netherlands: Kluwer Academic Publishers. https://doi.org/10.1007/978-94-009-3027-8

Turner, D. D., Wulfmeyer, V., & Schween, L. K. B. J. H. (2014). Water vapor turbulence profiles in stationary continental convective mixed layers. *Journal of Geophysical Research – Atmospheres*, *119*(19), 11,151–11,165. https://doi.org/10.1002/2014JD022202

van Heerwaarden, C. C., van Stratum, B. J. H., & Heus, T. (2017). microhh/microhh: 1.0.0 (Version 1.0.0) . *Zenodo*. doi: http://doi.org/10. 5281/zenodo.822842

van Heerwaarden, C. C., van Stratum, B. J. H., Heus, T., Gibbs, J. A., Fedorovich, E., & Mellado, J. P. (2017). Microhh 1.0: A computational fluid dynamics code for direct numerical simulation and large-eddy simulation of atmospheric boundary layer flows. *Geoscientific Model Development*, *10*(8), 3145–3165. https://doi.org/10.5194/gmd-10-3145-2017

van Zanten, M., et al. (2011). Controls on precipitation and cloudiness in simulations of trade-wind cumulus as observed during RICO. *Journal of Advances in Modeling Earth Systems*, *3*, 19.

Weckwerth, T. M. (2000). The effect of small-scale moisture variability on thunderstorm initiation. *Journal of the Atmospheric Sciences*, *128*, 4017–4030. https://doi.org/10.1175/1520-0493(2000)129

Wulfmeyer, V. (1999). Investigations of humidity skewness and variance profiles in the convective boundary layer and comparison of the latter with large eddy simulation results. *Journal of the Atmospheric Sciences*, *56*(8), 1077–1087. https://doi.org/10.1175/1520-0469 (1999)056<1077:IOHSAV>2.0.CO;2

Zhou, X., Heus, T., & Kollias, P. (2017). Influences of drizzle on stratocumulus cloudiness and organization. *Journal of Geophysical Research – Atmospheres*, *122*(13), 6989–7003. https://doi.org/10.1002/2017JD026641